Enhanced structural and magnetic properties of Al–Cr-substituted SrFe$_{12}$O$_{19}$ hexaferrite system

K. Subrahmanya Sarma[1] · Ch. Rambabu[1] · G. Vishnu Priya[1] · M. K. Raju[2] · D. Parajuli[3] · Batoo Khalid Mujasam[4] · Verma Ritesh[5] · Kumar Rajesh[5] · N. Murali[6] · P. V. Lakshminarayana[1]

Abstract

M-type Al–Cr-substituted strontium hexaferrite (SrFe$_{12-x-y}$Al$_x$Cr$_y$O$_{19}$ where x = y = 0.0, 0.05, 0.1, 0.15, and 0.2) powders are synthesized successfully using sol–gel auto-combustion method. The synthesized powders were sintered at 1200 °C for 2 h, and their structural, morphological, and magnetic properties were studied using characterization techniques like XRD (X-ray diffraction), FTIR (Fourier transform infrared spectroscopy), SEM (scanning electron microscopy), and VSM (vibrating sample magnetometer). The XRD pattern confirmed the formation of single phase hexagonal structure with P6$_3$/*mmc* space group. The saturation magnetization is observed to decrease from 63.37 to 46.89 emu/g with the increase in dopant concentration. However, the coercivity initially decreased and then increased with increase in dopant concentration.

Keywords Strontium nanohexaferrite · Saturation magnetization · XRD · FESEM · Coercivity

1 Introduction

The use of technology began with the transformation of natural resources into simple and smart tools. The prehistoric discovery of magnetic material in the form of lodestone and the later developments in ferromagnetic materials set the stage for microwave ferrite devices [1–6]. Studies of magnetic materials with intense magnetic properties, giant electrical resistivity, and low losses are of great interest in todays' era [7–12]. There has been tremendous interest in advance and new applications of hexaferrite in the last decade [13]. This particularly targeted electronic devices for WMC (wireless and mobile communications), EMI (electromagnetic interference) and EMC (electromagnetic compatibility), electromagnetic wave absorbers, radar absorbing materials for stealth technologies, and composite materials for advanced technological applications [14–16]. The development of nanofibers, fiber orientation, and alignment effects in hexaferrite, fiber composites with carbon nanotubes (CNT), lead to the interest of many researchers in nanotechnology [17–22]. For electronic applications, bulk ferrites always remained the first preference as a magnetic material for various applications [23]. Still, recently nanomaterial in ferrites have emerged as a strong contender in this field of electronic applications [24]. Many researchers presented the applications of nanoferrites in a range of radio and microwave frequencies through their research [1]. A thorough characterization of these materials is required to use nanomaterials for applications discussed by various research groups. Thus, the knowledge of internal attributes is a prerequisite to understanding these materials' behavior and thus enabling them to be used at higher frequencies. The property of materials depends mostly on the composition of the sample, the operating frequency, distribution of substituted cations, and particle size. The physical properties of nanoparticles are also affected significantly by preparation [25–27].

✉ N. Murali
  muraliphdau@gmail.com

1 Department of Nuclear Physics, Andhra University, Visakhapatnam 530003, A. P, India

2 Department Physics, WISTM Engineering College, Pinagadi, Visakhapatnam, A.P, India

3 Research Center for Applied Science and Technology, Tribhuvan University, Kathmandu, Nepal

4 College of Science, King Saud University, P.O. Box-2455, Riyadh 11451, Saudi Arabia

5 School of Physics and Materials Science, Shoolini University, Bajhol, Solan, H.P 173229, India

6 Department of Engineering Physics, AUCE (A), Andhra University, Visakhapatnam, India
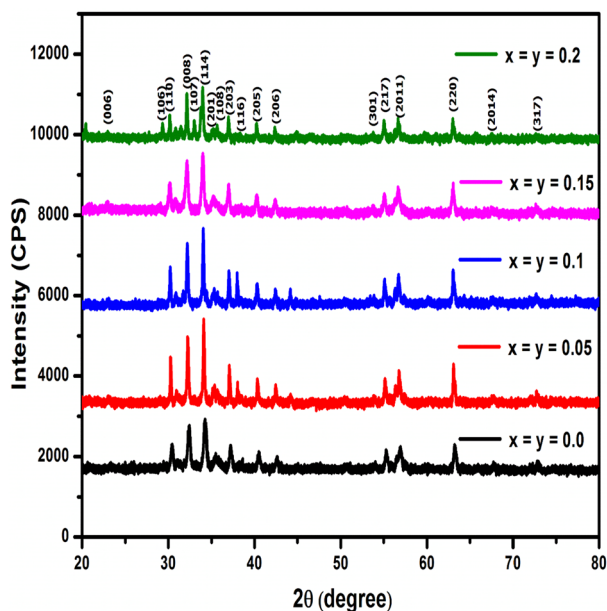
Fig. 1 X-ray powder diffraction for $SrFe_{12-x-y}Al_xCr_yO_{19}$ nanohexaferrites

However, there are numerous ferrites, ceramic oxides, dielectric oxides, etc., that have been utilized for various electronic and technological applications [28–38], but strontium hexaferrite has found demanding and competitive application with changing technology [39–42]. This is due to the favorable combination of adequate high magnetic properties, excellent physical and chemical stability, low production cost, easy availability of raw materials, and comparable high Curie temperature [43–45]. As a kind of hard magnetic material, the hexagonal ferrite material efficiency has the chemical formula of $MFe_{12}O_{19}$ (M = Ba, Sr, Pb) [46]. Various synthesis methods of M-type hexagonal ferrites were developed, including standard ceramic techniques, co-precipitation, ion exchange, sol–gel method, citrate synthesis, hydrothermal synthesis, glass crystallization, the combustion method, self-propagating high-temperature synthesis (SHS), spray drying, water-in-oil micro-emulsions, and industrial manufacture of hexagonal ferrites [47–53]. $SrFe_{12}O_{19}$ is a hard magnetic material due to its high coercivity. $SrFe_{12}O_{19}$

plays a relatively special role due to its appropriate magnetic properties, chemical stability, corrosion resistivity, and cost-efficiency compared to rare-earth compounds [54].

The Al–Cr compound is used as a dopant as other research groups minimally studied it. Thus, it is important to extract out maximum information about the effect of Al and Cr doping on $SrFe_{12}O_{19}$ which could be helpful for the application perspective. As the research work in the paper focuses on hexagonal ferrites. Further classification of hexagonal ferrite is done below: We represent a divalent ion such as magnesium, zinc, cobalt, and manganese: $SrFe_{12}O_{19}$ (M-type strontium hexaferrite), $(Sr_2Me_2Fe_{12}O_{22})$ Y-type ferrites, $(SrMe_2Fe_{16}O_{27})$ W-type ferrite, $(Sr_2Me_2Fe_{28}O_{46})$ X-type ferrites, $(Sr_4Me_2Fe_{36}O_{60})$ U-type ferrites [55, 56].

The main aim of this research is to acquire the Al–Cr-substituted strontium hexaferrite phase. The material, after pelletizing, is given a heat treatment at a temperature ($t = 1200$ °C) held for a duration of h in the furnace. The structure, morphological, and magnetic properties were studied for material synthesized by sol–gel auto-combustion technique.

2 Experimental details

The properties of the synthesized Al–Cr-doped strontium hexaferrite material depend upon the method of preparation and environmental conditions. In the present research, the synthesis of ferrite having compositional formula $SrFe_{12-x-y}Al_xCr_yO_{19}$ (where x = y = 0.0, 0.05, 0.1, 0.15, and 0.2) was carried out using sol–gel auto-combustion method. The sol–gel auto-combustion method is used due to the several advantages such as homogeneous particle distribution and small particle size formation. AR graded strontium nitrate $[Sr(NO_3)_2]$, aluminum nitrate $[Al(NO_3)_3]$, chromium nitrate $[Cr(NO_3)_3]$, ferric nitrate $[Fe(NO_3)_3 \cdot 9H_2O]$, citric acid $[C_6H_8O_7]$, and ammonia solution, with 99.9% purity, were taken as starting materials. Strontium and chromium nitrate are diluted into methanol and ferric nitrate into 10 mL of methanol. The solutions of all the nitrate salts are combined in a 250-mL beaker, with the aqueous solution of citric acid that acts as the chelating agent. The beaker is placed on

Table 1 Lattice parameters data of $SrFe_{12-x-y}Al_xCr_yO_{19}$ nanohexaferrites

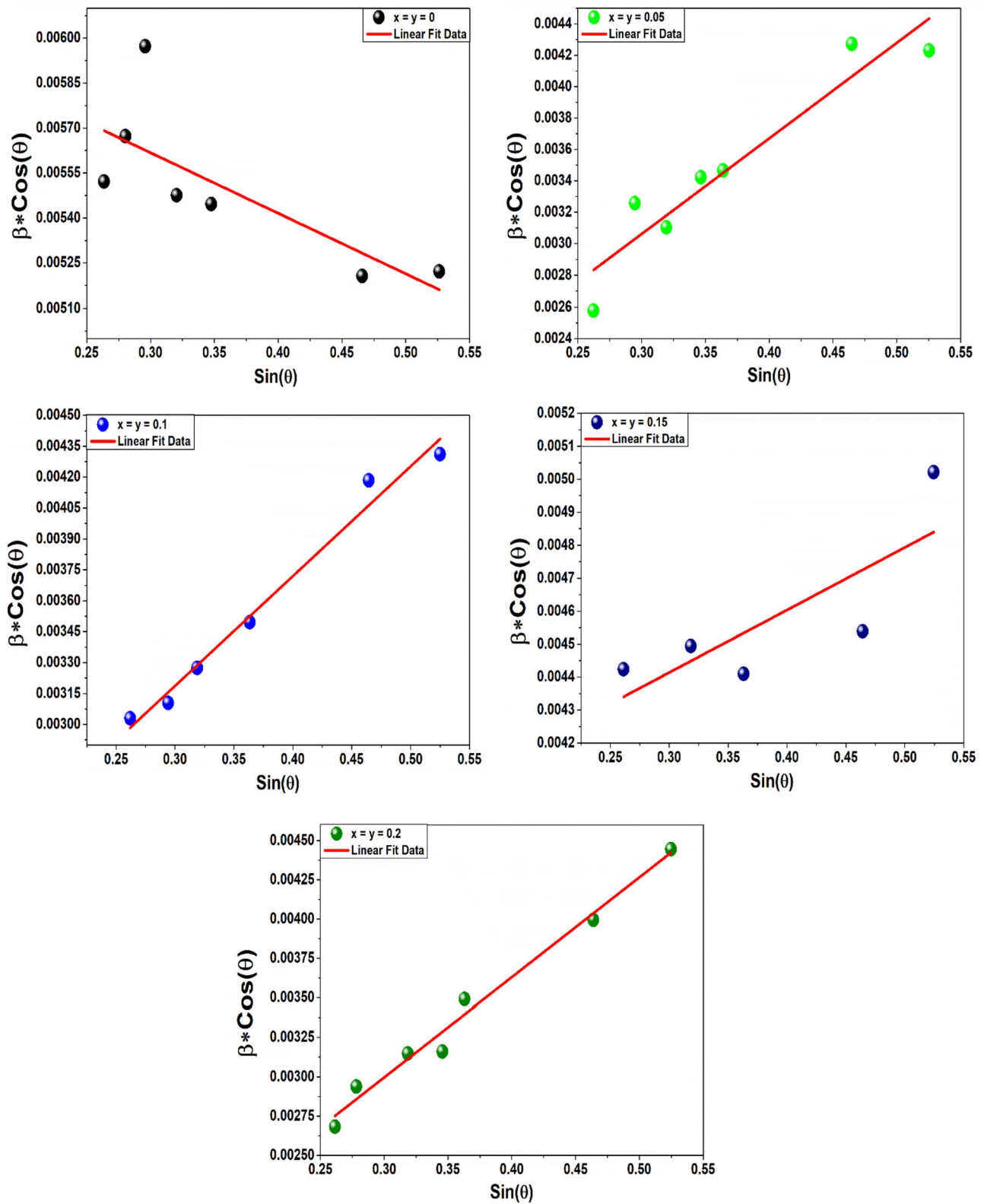| Structural parameters	Compounds (x = y)				
	0.0	0.05	0.1	0.15	0.2
a (Å)	5.896	5.893	5.890	5.886	5.882
c (Å)	23.041	22.995	22.983	22.967	22.949
c/a	3.9034	3.9025	3.9023	3.9016	3.9015
V(Å)^3	693.645	691.55	690.49	689.07	687.59
Crystallite size (nm) Scherrer method	36.28	32.39	29.65	27.74	21.81
Crystallite size (nm) W–H method	26.906	26.453	24.794	23.733	22.758

Fig. 2 Williamson–Hall plot for SrFe$_{12-x-y}$Al$_x$Cr$_y$O$_{19}$ nanohexaferrites

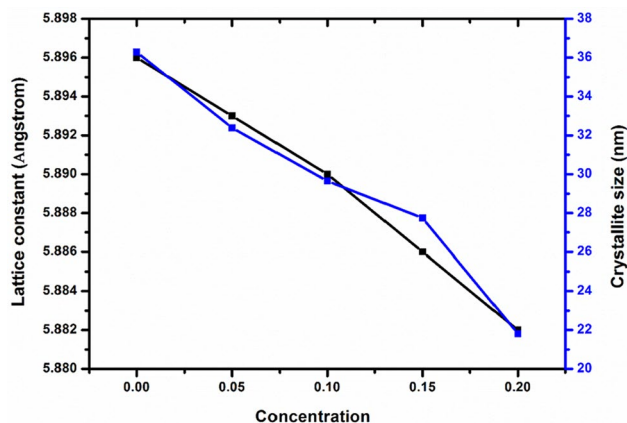**Fig. 3** Lattice constant versus crystallite size of $SrFe_{12-x-y}Al_xCr_yO_{19}$ nanohexaferrites

a hot plate with continuous stirring, maintaining at 80 °C. The solution changed into a viscous solution and finally to a thick viscous gel after evaporation. This constant stirring continued for nearly 12 to 18 h. The gel is converted to ash-colored powder on the removal of all water molecules from the mixture. This was followed by preheating at 900 °C for 2 h to remove the volatile compounds, and further heat treatment is carried out at 1200 °C at a rate of 5 °C per minute for 2 h to enhance the crystalline property.

Rigaku Cu-Kα diffractometer is used for powder X-ray diffraction (XRD) data of the sample with diffraction angles between 20° and 80° in increments of 0.02°. The least-square fitting method calculates the unit cell lattice parameter from the d-spacing and (*hkl*) values. By applying Scherrer's equation to the XRD pattern, the crystal size of the sample is obtained. Field effect scanning electron microscopy (FE-SEM) images are taken using Carl Zeiss, EVOMA 15, Oxford Instruments, and Inca Penta FETx3. JPG to derive the particle morphology of the powders. Fourier transform infrared (FTIR) spectra are obtained using Shimadzu FTIR-8900 spectrometer using the KBr pellet technique in the wavenumber range between 400 and 1000 cm^{-1}. VSM (Lakeshore 7300 USA) results were used to study the magnetic characteristics of the sample with an external field of 17 kOe.

3 Results and discussion

3.1 Structural studies

The presence of the major XRD peaks shown in Fig. 1 with (*hkl*) values of (110), (008), (107), (114), (203), (205), (217), and (220) confirms the hexagonal structure of the substituted

materials. XRD patterns for $SrFe_{12-x-y}Al_xCr_yO_{19}$ where x = y = 0.0, 0.05, 0.1, 0.15, and 0.2 are obtained. The Al–Cr-doped strontium hexaferrite heat-treated at 1200 °C/ 2 h was investigated using the X-ray diffractometer technique. They agree with the JCPDS pattern with reference codes #33-1340 [57]. These XRD results accustomed the promising substitution of Al–Cr ions in place of Fe^{3+} ions on interstitial sites of $SrFe_{12}O_{19}$ lattice as no other peak was detected. The analysis reveals that the substituted compound has almost the same pattern as that of pure form. The observations were used to calculate the crystallite size from the XRD graphs using Debye's Scherrer equation and Williamson–Hall plot (W–H method) and are given in Table 1. Table 1 gives the calculated crystallite size of the particles, which shows two type of changes. One is that the crystallite size decreases with the increase in doping concentration from both the methods [58]. The crystallite size obtained from Scherrer method is greater than that of the size obtained from W–H method which is because Williamson–Hall method takes microstrain into consideration [59] (Fig. 2). The decrease in average crystallite size is due to the doping of Al and Cr, due to which the average bond length decreases and hence results in the growth of smaller crystallites. The second observation was that with an increase in dopant concentration, the lattice constant decreases, as shown in Fig. 3. The decrease in lattice constant may be due to the lower ionic radii of Al^{3+} (0.535 Å) and Cr^{3+} (0.520 Å) than that of Fe^{3+} (0.645 Å) [50]. The decrease in lattice constant with an increase in Al–Cr content x obeys Vegard's law [60]. This is because of Vegard's law, where the lattice parameter varies linearly from Fig. 3. This can be because the atomic size of Al–Cr is more than that of iron ions.

The lattice parameters for the diffraction composition of the given series have been calculated using Bragg's law [61], and the lattice constants a and c were calculated using the following equation [62];

$$\frac{1}{d^2} = \frac{4}{3}\left(\frac{h^2 + hk + k^2}{a^2}\right) + \frac{l^2}{c^2}$$

where *d* is the crystal face distance and (*hkl*) is the Miller indices.

The average crystallite size (*t*) was calculated using the Scherrer formula [63], for which the most intense peak (114) of the XRD pattern was considered;

$$t = \frac{0.9\lambda}{\beta\cos\theta}$$

K is the wavelength of the Cu-Ka radiation, *b* is the full width of the half maximum, and *h* is Bragg's angle.

In order to confirm the structural and phase purity, Rietveld refinement is performed using FullProf software till the convergence reached 2, as shown in Fig. 4. It is noted
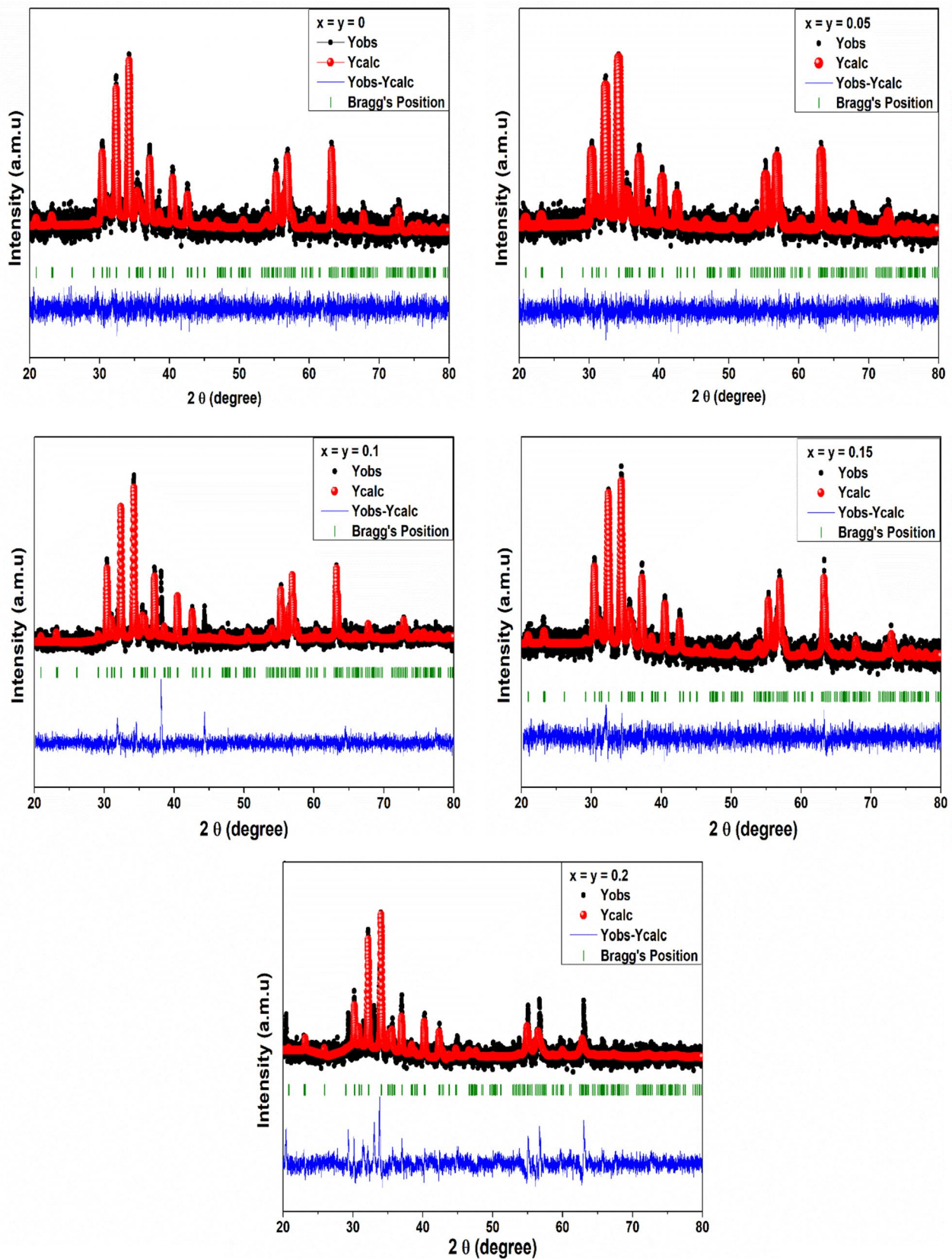
Fig. 4 Rietveld refinement pattern for SrFe$_{12-x-y}$Al$_x$Cr$_y$O$_{19}$ nanohexaferrites

Table 2 Rietveld refinment parameters for $SrFe_{12-x-y}Al_xCr_yO_{19}$ nanohexaferrites

Composition $x = y$	X^2	R_{wp}	R_{exp}	R_p
0	1.136	36.3	34.0	69.8
0.05	1.13	36.4	34.2	69.9
0.1	1.702	39.9	30.6	75.0
0.15	1.198	33.7	30.8	58.9
0.2	1.997	41.2	37.3	82.3

that all sample shows the formation of hexagonal structure at room temperature. The relevance factor calculated for all the samples is shown in Table 2.

4 FESEM results

Figure 5 presents SEM images of the prepared $SrFe_{12-x-y}Al_xCr_yO_{19}$ (where x = y = 0.0, 0.05, 0.1, 0.15, and 0.2) nanohexaferrite samples. It is observed from FESEM images that the synthesized samples appear to be a mixture of individual nanoparticles of a well crystalline nature and aggregates formed as a result of the agglomeration of individual nanoparticles. All grains are observed to have a hexagonal morphology, which is in consistent with the literature survey [64]. In addition, the grains are non-homogeneous in nature which could be due to the oxygen vacancy formation. However, the grain size is observed to decrease with the increase in dopant concentration which is because Al^{2+} ions are diamagnetic in nature and hence reduce the magnetic interaction between the two particles.

5 FTIR Spectroscopy

In Fig. 6, the characteristic intense peaks can be seen. We observed that the transmittance in the $SrFe_{12-x-y}Al_xCr_yO_{19}$ where x = y = 0.0, 0.05, 0.1, 0.15, and 0.2 hexaferrite samples. The result exhibits three impressive transmittance peaks of strontium hexaferrite at ~ 407.256 cm^{-1} to 411.658 cm^{-1} which align with the work published by other researchers [43, 65]. The spectrums show the hydroxyl at about 3420 cm^{-1}. The peaks at a wavelength less than 600 cm^{-1} are also due to the iron oxide. It is noticeable in the sample of Al–Cr-doped strontium hexaferrite. The figures showed that transmittance occurs at 551.256 cm^{-1} to 584.014 cm^{-1} according to distinctive M–O bonds of $SrFe_{12-x-y}Al_xCr_yO_{19}$. It also indicates that the transmission peaks fall with $SrFe_{12-x-y}Al_xCr_yO_{19}$, thus stating absorption.

6 Magnetic properties

The magnetization hysteresis loops of $SrFe_{12-x-y}Al_xCr_yO_{19}$ (where x = y = 0.0, 0.05, 0.1, 0.15, and 0.2) hexaferrite samples are shown in Fig. 7. The remanence and saturation magnetization decrease with an increase in substitution of Al–Cr ions, as shown in Table 2, giving the values of M_s, H_c, M_r at all concentration levels. The nano-sized particles have almost the same XRD pattern, which shows that they keep the same crystalline structure [66]. This confers that this change in magnetic property is not because of a change in crystal structure but because of the domain size of hexagonal ferrites [38]. The maximum limit for the single magnetic domain should have a size of 100 nm. The ferrite particle with a size less than a single domain size will lower ferromagnetic resonance frequency [67]. The entire particle with internal magnetization comparable to the single domain limit gets aligned and reduces the system energy to its minimum value. The improved saturation magnetization and better coercivity than other works make these hexagonal ferrites competent materials in magnetic devices and electromagnetic wave absorption material [68, 69].

Magnetic properties changed appreciably after the substitution of Al–Cr ions in $SrFe_{12}O_{19}$. The remenance decreases to a great extent on the addition of Al–Cr ions until a concentration of 4%. At the same time, the coercivity changes slightly in a significant increase in curve slope, as shown in Fig. 8. The magnetization curve of the $SrFe_{12-x-y}Al_xCr_yO_{19}$ (x = 0.0–0.2) shows ferromagnetic properties saturated under a field of 15 KOe. It also indicates remanent magnetization (M_r) approaches from 43.22 to 28.22 emu/g, and saturation magnetization (M_s) approaches from 62.37 to 46.89 emu/g. With the initial increase in Al–Cr ions level, decrease in the M_s and M_r is also reported by Chawla in his findings [70]. When x = 0.2, the M_s and M_r drop-down, respectively, as indicated in Fig. 9, indicating that the higher concentration of Al–Cr ions substitution reduces the magnetic property as doped ions occupy ferromagnetically ordered tetrahedral and octahedral sites to weaken spin interactions [71] (Table 3).

7 Conclusion

Nanostructure strontium hexaferrite substituting Al–Cr ($SrFe_{12-x-y}Al_xCr_yO_{19}$) nanohexaferrites for a concentration of 0.0, 0.05, 0.1, 0.15, and 0.2 has been successfully synthesized by sol–gel auto combustion method. The prepared powders were sintered at 1200 °C /2 h. XRD patterns revealed that the particles are nano-sized and confirm single-phase hexagonal magnetoplumbite in structure with a space group of $P6_3/mmc$. The crystallite size is observed
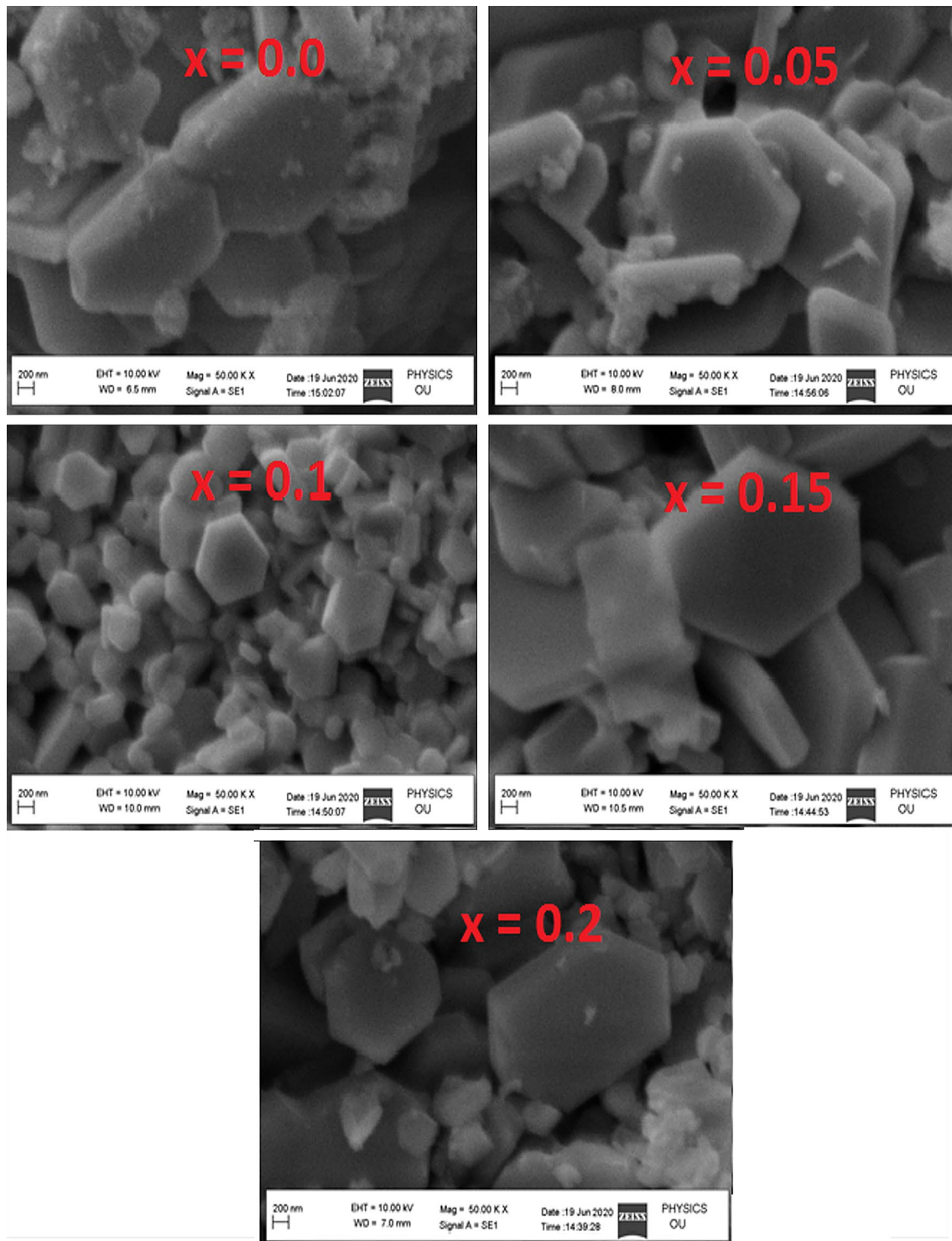
Fig. 5 FESEM images for SrFe$_{12-x-y}$Al$_x$Cr$_y$O$_{19}$ nanohexaferrites

to decrease from 36.28 to 21.81 nm by Scherrer method and from 29.906 to 22.758 nm by Williamson–Hall method, with the increase in dopant concentration. The SEM images of the produced ferrite present a low agglomeration rate of particles and grain sizes in the proximity of 150–380 nm. The FTIR analysis confirmed the presence of hexagonal structure without any impurity phase formation. The magnetic properties like saturation magnetization M$_s$ and coercivity H$_c$ varied from 62.37 to 46.89 emu/g and 3843.88 Oe to 4826.10 Oe, respectively.
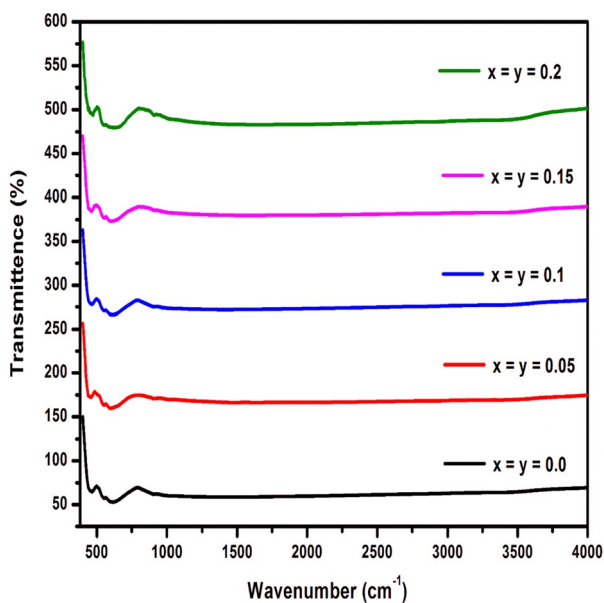
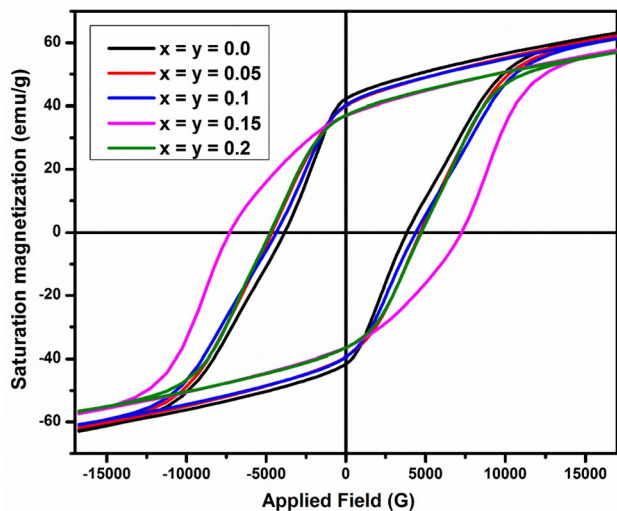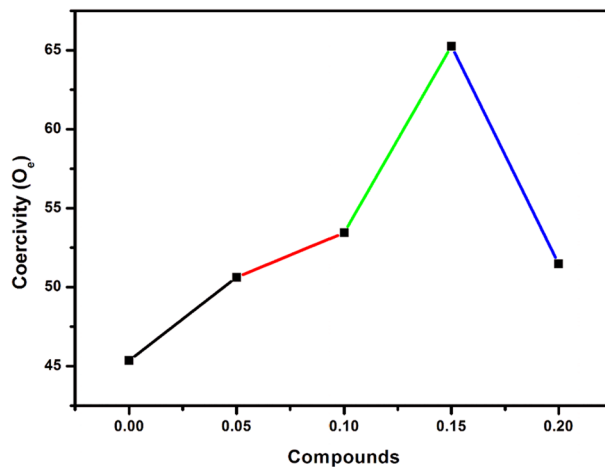**Fig. 6** Infrared spectra of $SrFe_{12-x-y}Al_xCr_yO_{19}$ nanohexaferrites

Fig. 8 Coercivity (Hc) graph of $SrFe_{12-x-y}Al_xCr_yO_{19}$ nanohexaferrites

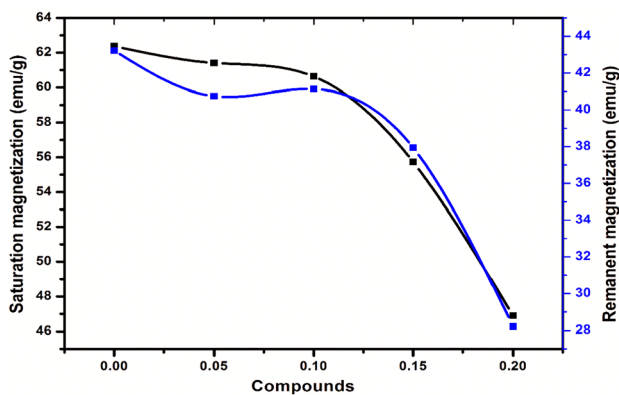**Fig. 9** Saturation magnetization (Ms) versus remanent magnetization (M_r) graph of $SrFe_{12-x-y}Al_xCr_yO_{19}$ nanohexaferrites

Fig. 7 Hysteresis curve of $SrFe_{12-x-y}Al_xCr_yO_{19}$ nanohexaferrites

Table 3 Saturation magnetization (M_s), remanent magnetization (M_r), and coercivity (Hc) data of $SrFe_{12-x-y}Al_xCr_yO_{19}$ nanohexaferrites

Magnetization parameter	Compounds (x = y)				
	0.0	0.05	0.1	0.15	0.2
M_s (emu/g)	62.37	61.41	60.63	55.73	46.89
M_r (emu/g)	43.22	40.74	41.13	37.94	28.22
H_c (Oe)	3843.88	4169.44	4019.99	4826.10	4273.88
M_r/M_s	0.69	0.66	0.68	0.68	0.60

References

1. Mulushoa, S. Yonatan, N. Murali, M. Tulu Wegayehu, V. Veeraiah, K. Samatha, Mater. Today: Proc. **5**(13), 26460–26468 (2018).

2. Mulushoa, S. Yonatan, Ch. Vijaya Kumari, V. Raghavendra, K. Ephraim Babu, B.S.N. Murthy, K. Suribabu, Y. Ramakrishna, N. Murali, Phys. B: Condensed Matter **572**, 139–147 (2019).

3. Mercy, S. Jesus, N. Murali, A. Ramakrishna, Y. Ramakrishna, V. Veeraiah, K. Samatha, Appl. Phys. A **126**(11), 1–13 (2020).

4. P. Himakar, K. Jayadev, D. Parajuli, N. Murali, P. Taddesse, S. Yonatan Mulushoa, T. Wegayehu Mammo, B. Kishore Babu, V. Veeraiah, K. Samatha, Appl. Phys. A **127**(5), 1–10 (2021).

5. P. Himakar, N. Murali, D. Parajuli, V. Veeraiah, K. Samatha, T.W. Mammo, K.M. Batoo, M. Hadi, E.H. Raslan, S.F. Adil, J. Electron. Mater. **50**(6), 3758–3758 (2021)

6. B. Madhavilatha, D. Parajuli, K. Jayadev, Ch. Komali, N. Murali, V. Veeraiah, K. Samatha, Biointerface Res. Appl. Chem. **12**(2), 1899–1906 (2021).

7. K. Chandramouli, B. Suryanarayana, P.V.S.K. Phanidhar Varma, V. Raghavendra, K.A. Emmanuel, P. Taddesse, N. Murali, T. Wegayehu Mammo, D. Parajuli, Results Phys. **24**, 104117 (2021).

8. K. Chandramouli, P. Anantha Rao, B. Suryanarayana, V. Raghavendra, S. Jesus Mercy, D. Parajuli, P. Taddesse, S. Yonatan Mulushoa, T. Wegayehu Mammo, N. Murali, J. Mater. Sci.: Mater. Electron. **32**, 15754–15762 (2021).

9. D. Parajuli, V. Raghavendra, B. Suryanarayana, P. Anantha Rao, N. Murali, P.V.S.K. Phanidhar Varma, R. Giri Prasad, Y. Ramakrishna, K. Chandramouli, Results Phys. **23**, 103947 (2021).

10. K. Ramanjaneyulu, B. Suryanarayana, V. Raghavendra, N. Murali, D. Parajuli, K. Chandramouli, Solid State Technol. **64**(2), 7192–7200 (2021)

11. PVSK Phanidhar Varma, V. Raghavendra, D. Parajuli, N. Murali, K. Chandramouli, Solid State Technol. **63**(5), 8820–8827 (2020).

12. S. Kuswanth Kumar, N. Murali, D. Parajuli, A. Ramakrishna, P.S.V. Subba Rao, M.P. Rao, Solid State Technol. **63**(5), 4069–4077 (2020).

13. Z.W. Geng, M. Haseeb, X.K. Quan, B.S. Li, W.Q. Liu, G.H. Hu, W.Q. Sun, M. Yue, R.M. Liu, Mater. Res. Express **7**(4), 046107 (2020).

14. Karahroudi, Z. Hajian, K. Hedayati, M. Goodarzi, Main Group Met. Chem. **43**(1), 26–42 (2020).

15. P.N. Anantharamaiah, N. Sarath Chandra, H. M. Shashanka, R. Kumar, B. Sahoo, Adv. Powder Technol. **31**(6), 2385–2393 (2020).

16. İ.Ç.İ.N. Kürşat, S. Öztürk, D.D. Çakil, S.E. Sünbül, J. Alloys Compd. **873**, 159787 (2021).

17. K. Chandramouli, V. Raghavendra, P.V.S.K. Phanidhar Varma, B. Suryanarayana, T. Wegayehu Mammo, D. Parajuli, P. Taddesse, N. Murali, Appl. Phys. A **127**, 596 (2021).

18. N. Madubuonu, S.O. Aisida, I. Ahmad, S. Botha, T.K. Zhao, M. Maaza, F.I. Ezema, Appl. Phys. A **126**, 72 (2020)

19. S.O. Aisida, I. Ahmad, T.K. Zhao, M. Maaza, F.I. Ezema, J. Macromol.r Sci.: Part B **59**, 295–308 (2020)

20. S.O. Aisida, I. Ahmad, F.I. Ezema, Phys. B: Condensed Matter **579**, 411907 (2020).

21. S.O. Aisida, P.A. Akpa, I. Ahmad, M. Maaza, F.I. Ezema, Physica B **571**, 130–136 (2020)

22. S.O. Aisida, A. Ali, O.E. Oyewande, I. Ahmad, A. Ul-Hamid, T.K. Zhao, M. Maaza, F.I. Ezema, J. Nanopart. Res. **23**, 47 (2021)

23. A. Ramakrishna, N. Murali, S.J. Margarette, K. Samatha, V. Veeraiah, Physica B **530**, 251–257 (2018)

24. N. Murali, S.J. Margarette, G. Pavan Kumar, B. Sailaja, S. Yonatan Mulushoa, P. Himakar, B. Kishore Babu, V. Veeraiah, Phys. B: Condensed Matter **522**, 1–6 (2017).

25. Mammo, T. Wegayehu, N. Murali, Y. Mulushoa Sileshi, T. Arunamani, Phys. B: Condensed Matter **531**, 164–170 (2018).

26. M.L. Ghimire, D.L. Kunwar, J.N. Dahal, D. Neupane, S. Yoon, S.R. Mishra, Mater. Sci. Appl. **11**(7), 474–493 (2020)

27. M.A. Almessiere, Y. Slimani, S. Guner, M. Sertkal, A.D. Korkmaz, S.E. Shirsath, A. Baykal. Ultrasonics Sonochem. **58**, 104654 (2019).

28. A. Hamrita, Y. Slimani, M.K.B. Salam, E. Hannachi, L. Bessais, F.B. Azzouz, M.B. Salem, Ceram. Int. **40**, 1461–1470 (2014)

29. Y. Slmani, E. Hannachi, M.K.B. Salem, F.B. Azzouz, M.B. Salem, Appl. Phys. A **124**, 91 (2018)

30. M.K.B. Salem, A. Hamrita, E. Hannachi, Y. Slimani, M.B. Salem, F.B. Azzouz, Phys. C: Superconduct. **498**, 38–44 (2014)

31. E. Hannachi, Y. Slimani, A. Ekicibil, A. Manikandan, F.B. Azzouz, Mater. Chem. Phys. **235**, 121721 (2019).

32. K. Seevaken, A. Manikandan, P.D. Devendran, Y. Slimani, A. Baykal, T. Alagesan, J. Magn. Magn. Mater. **486**, 165254 (2019).

33. R. Verma, A. Chauhan, K.M. Batoo, R. Jasrotia, A. Sharma, R. Kumar, M. Hadi, E.H. Raslan, J.P. Labis, A. Imran, ECS J. Solid-State Tech. **10**, 073004 (2021).

34. R. Verma, A. Chauhan, K.M. Batoo, M. Hadi, E.H. Raslan, R. Kumar, M.F. Ijaz, A.K. Assaifan. J. Alloy Compd. **869**, 159520 (2021).

35. R. Verma, A. Chauhan, K.M. Batoo, R. Kumar, M. Hadi, E.H. Raslan, Ceram. Int. **47**, 15442–15457 (2021).

36. K.M. Batoo, R. Verma, A. Chauhan, R. Kumar, M. Hadi, O.M. Aldossary, Y. Al-Douri, J. Alloy Compd. **883**, 160836 (2021).

37. M. Shandilya, R. Verma, J. Magn. Magn. Mater. **527**, 167782 (2021).

38. S. Gulbadan, S. Rabia Ejaz, A. Hussain Nizamani, I. Shakir, P. Olaleye Agboola, M. Niaz Akhtar, M. Farooq Warsi, M. Azhar Khan, Ceram. Int. **46**(4), 4914–4923 (2020).

39. Starikov, A. Yu, D.A. Vinnik, S.A. Gudkova, Russ. Internet J. Ind. Eng. **7**(1), 30–34 (2020).

40. M.A. Almessiere, Y. Slimani, A. Baykal, Ceram. Int. **28**, 407–417 (2017)

41. M.A. Almessiere, Y. Slimani, H.S. El-Sayed, A. Baykal, I. Ercan, J. Magn. Magn. Mater. **471**, 124–132 (2019)

42. S. Guner, M.A. Almessiere, Y. Slimani, A. Baykal, I. Ercan, Ceram. Int. **46**, 4610–4618 (2020).

43. T.P. Poudel, D. Guragain, J. Mohapatra, J.P. Liu, S.R. Mishra, J. Nanosci. Nanotechnol. **20**(12), 7735–7742 (2020)

44. S.S. Kumar, R.K. Singh, A. Manash, G. Kumar, U. Shankar, H.K. Satyapal, in IOP Conference Series: Materials Science and Engineering, vol. 1149, no. 1, p. 012013. IOP Publishing (2021).

45. A. Thakur, V. Kumar, J. Nanomater. Sci. **4**, 06–10 (2020)

46. T. Jayakumar, R. Aarthi, C. Ramachandra Raja, S. Arumugam, J. Superconduct. Novel Magn. **33**(12), 3937–3940 (2020).

47. S.E. Shirsath, R.H. Kadam, K.M. Batoo, D. Wang, S. Li, J. Phys. D: Appl. Phys. **54**(2), 024001 (2020).

48. Mahmood, M. Adil, A. Majeed, T. Zelai, T.I. Al-Muhimeed, A.A. AlObaid, M. Morsi, H. Albalawi, U. Ayaz, M. Azhar Khan, Ceram. Int. (2021).

49. G.A. Al-Garalleh, S.H. Mahmood, I. Bsoul, R. Loloee, Mater. Res. Express **7**(2), 026103 (2020).

50. Y. Slimani, M.A. Almessiere, S. Guner, F.S. Alahmari, G. Yasin, A.V. Trukhanov, A. Baykal, Mater. Chem. Phys. **253**, 123324 (2020).

51. M.A. Almessiere, Y. Slimani, A.D. Korkmaz, A. Baykal, H. Albetran, T.A. Saleh, M. Sertkol, I. Ercan, Ultrasonic Sonochem. **62**, 104847 (2020).

52. M.A. Almessiere, Y. Slimani, M. Sertkol, M. Nawaz, A. Baykal, I. Ercan, Results Phys. **13**, 102244 (2019).

53. M.A. Almessiere, Y. Slimani, H.S. El-Sayed, A. Baykal, J. Sol-Gel. Sci. Technol. **88**, 628–638 (2018)

54. A. Majeed, M. Azhar Khan, M. Yousuf Lodhi, R. Ahmad, I. Ahmad, Ceram. Int. **46**(2), 1907–1915 (2020)

55. M. Junaid, M. Nadeem, S.A. Abubshait, H.A. Abubshait, M. Azhar Khan, Z. Abbas Gilani, M. Farooq Warsi, Ceram. Int. **46**(16), 25478–25484 (2020).

56. R. Jasrotia, P. Puri, V. Pratap Singh, R. Kumar, J. Sol–Gel Sci. Technol. **97**(1), 205–212 (2021).

57. S. Du, H. Chen, R. Hong, Nanotechnol. Rev. **9**(1), 105–114 (2020)

58. D.E. Zhivulin, D.A. Vinnik, O.V. Zaitseva, Russ. Internet J. Ind. Eng. **7**(1), 19–25 (2020).

59. R. Verma, A. Chauhan, K.M. Batoo, R. Kumar, M. Hadhi, E.H. Raslan, Ceram. Int. **47**, 3680–3691 (2020)

60. Y. Slimani, B. Unal, M.A. Almessiere, A. Demir Korkmaz, A. Baykal, Mater. Chem. Phys. **260**, 124162 (2021).

61. A. Hashhash, A. Hassen, W.S. Baleidy, H.S. Refai, J. Alloys Compd. **873**, 159812 (2021).

62. Y.H. Hou, X. Chen, X.L. Guo, W. Li, Y.L. Huang, X.M. Tao, J. Magn. Magn. Mater. 168257 (2021).

63. T. Jayakumar, C. Ramachandra Raja, S. Arumugam, J. Magn. Magn. Mater. **33**(8), 2451–2458 (2020).

64. Adi, W. Ari, Y. Yunasfi, Y. Sarwanto, M. Aziz Majidi, Vacuum **177**, 109436 (2020). ogi 82, no. 4 (2020).

65. M. Hadi, K.M. Batoo, A. Chauhan, O.M. Aldossary, R. Verma, Y. Yang, Megnetochemistry **7**, 53 (2021)

66. P. Jenuš, A. Učakar, S. Repše, C. Sangregorio, M. Petrecca, M. Albino, R. Cabassi, C. de Julián Fernández, B. Belec, J. Phys. D: Appl. Phys. **54**(20), 204002 (2021).

67. M. Effendi, E. Solihah, C. Kurniawan, W. Cahyanto, W. Widanarto, in Key Engineering Materials, vol. 855, pp. 255–260. Trans Tech Publications Ltd (2020).

68. P. Kaur, S. Bahel, S. Bindra Narang, J. Electron. Mater. **49**(3), 1654–1659 (2020).

69. K.M. Batoo, M. Hadi, R. Verma, A. Chauhan, R. Kumar, M. Singh, O.M. Aldossary, Ceram. Int. (2021).

70. M.Effendi, E. Nugraha, W. Tri Cahyanto, W. Widanarto, in Journal of Physics: Conference Series, vol. 1494, no. 1, p. 012042. IOP Publishing (2020).

71. S. Selvaraj, U. Gandhi, L. John Berchmans, U. Mangalanathan, Mater. Technol. **36**(1), 36–45 (2021).